This is a preprint, the final version is subject to change, of the American Mineralogist (MSA)
Cite as Authors (Year) Title. American Mineralogist, in press.
(DOI will not work until issue is live.) DOI: http://dx.doi.org/10.2138/am-2017-6148

Revision 1 (6148)

A qualitative and quantitative investigation of partitioning and local structure of arsenate in barite lattice during co-precipitation of barium, sulfate and arsenate

XU MA[1,2], ZIDAN YUAN[1], MARIO A. GOMEZ[3,4], XIN WANG[1], SHAOFENG WANG[1,*], SHUHUA YAO[3], AND YONGFENG JIA[1,3,*]

[1]Key Laboratory of Pollution Ecology and Environmental Engineering, Institute of Applied Ecology, Chinese Academy of Sciences, Shenyang, China, 110016, China

[2]University of Chinese Academy of Sciences, Beijing, China 100049, China

[3]Institute of Environmental Protection, Shenyang University of Chemical Technology, Shenyang, China, 110142, China

[4]Department of Mining and Materials Engineering, McGill University, 3610 University Street, Montreal, Canada

The corresponding author: Dr. Shaofeng Wang, Email: wangshaofeng@iae.ac.cn; Telephone: +86 24 83970502; Fax: +86 24 83970503, Prof. Yongfeng Jia, Email: yongfeng.jia@iae.ac.cn; Telephone: +86 24 83970503; Fax: +86 24 83970503

ABSTRACT

Arsenic (As), barium (Ba), and sulfate (SO_4^{2-}), co-existing in natural and mining impacted environments, possibly lead to As-barite co-precipitation. This work investigated the co-precipitation of Ba^{2+}, SO_4^{2-} and AsO_4^{3-} (As(V)) and the incorporation of As(V) into the barite structure. The As(V) content in the coprecipitates increased with pH and the initial aqueous As(V) concentration. At pH ≤ 5, As(V) was dominantly fixed through isomorphic substitution for SO_4^{2-} in the barite structure (< 0.32 wt. %). At pH > 5, barium (hydrogen) arsenate constituted an appreciable fraction of As(V)-bearing species in addition to the incorporated As(V). FTIR spectroscopy indicated that As(V) in the coprecipitate occurred as mixed phases and the As(V) species incorporated into the barite structure was dominated by $HAsO_4^{2-}$ species. EXAFS analysis gave As-O and As-OH bond lengths of 1.67 Å and 1.75 Å for $HAsO_4^{2-}$ in barite structure, respectively. The FPMS structural refinement reproduced well the As *K*-edge XANES spectrum and gave bond lengths of As-O at 1.63, 1.64, 1.68, and 1.75 Å with an average bond length of 1.68 ± 0.05 Å in $HAsO_4^{2-}$ doped barite structure. The findings are of significance for understanding the geochemical cycle of As in As(V), Ba^{2+}, SO_4^{2-} co-existing systems.

Keywords: Arsenate, barite, co-precipitation, incorporation, local structure, XANES/EXAFS, FTIR, DFT calculation

INTRODUCTION

Given the toxicity of arsenic (As), a wide range of studies have been undertaken on its transformation, mobilization, and fixation in various environments. Besides As sorption/desorption on the surface of metal oxide/clay minerals and precipitation/dissolution of As-containing minerals (Das et al. 1996; Nickson et al. 1998; Acharyya et al. 1999; Sherman and Randall 2003), incorporation of As into minerals is also one of the most important processes/mechanisms influencing As mobility in natural and mining environments (Savage et al. 2005; Dutrizac and Jambor 2007; Fernández-Martínez et al. 2008; Lee et al. 2009; Gomez et al. 2010, 2011 2013a, 2013b; Kendall et al. 2013; Lin et al. 2013a, 2013b; Sunyer et al. 2013; Zhang. et al. 2015; Wang et al., 2017). It has been found that isomorphic substitution of arsenate (As(V)) for sulfate, phosphate and vanadate positions in mineral structures is widely occurring in hydrometallurgical tailings, As-rich mine waters and natural sediments, which can potentially influence the mobility, bioavailability, and transformation of As(V) (Sunyer et al. 2013; Zhang. et al. 2015; Muehe et al. 2016).

Barite could form in some geological environments (e.g. deep-sea, groundwater, river, hot spring water, and crust deposits) and mining related areas that contain considerable amounts of As (Goodarzi 2002; McBeth et al. 2003; Pone et al. 2007; Arik and Sgem 2008; Romero et al. 2010; Liu and Hendry 2011; Gomez et al. 2013a). For instance, barite precipitated from hot spring water and mining areas where As(III) was oxidized as As(V) in the thermal and aerobic environment (Villanueva et al. 2013; Tokunaga et al. 2016). Barite is used as a solubility control of ^{226}Ra in the

neutralization of acidic As containing sulfate rich hydrometallurgical raffinate solutions in Canada's uranium industry (Liu and Hendry 2011). These processes may lead to the formation of an As(V)-barite coprecipitate and incorporation of As(V) into the crystal lattice of barite. Tokunaga et al. reported that the concentration of As incorporated into natural barite could reach up to 24.3 $mg \cdot kg^{-1}$ in an Okinawa hydrothermal vent and was in the range of 5.25 – 438 $mg \cdot kg^{-1}$ in the laboratory coprecipitates (Tokunaga et al. 2016). In their work, they focused on the influence of As oxidation state in natural barite on its immobilization and the ratio of As(III)/As(V) as an indicator for sub-oxic/anoxic redox conditions. However, the dominant As(V) species (e.g. protonated or not), which strongly influence the amount of As fixed by barite, the local atomic structure of As(V) in the barite crystal lattice, and the possible barium arsenate phases formed are still unclear.

The objectives of the present work were to qualitatively and quantitatively study the amount and species of the As(V) in solid phase and its structure in barite during the co-precipitation of As(V), Ba, and SO_4^{2-} at various pH's and initial As(V) concentrations.

MATERIALS AND METHODS

All chemicals used in this work were of analytical grade and used without further purification. De-ionized (DI) water was used for all experiments.

Synthesis of standard materials

As(V)-free barite was precipitated by mixing a CO_2-free 0.2 mol L^{-1} barium solution (from $BaCl_2 \cdot 2H_2O$) and a 0.2 mol L^{-1} sulfate solution (from Na_2SO_4) at a pH

of 7.0 using 0.01 M NaOH as a base. Barium hydrogen arsenate ($BaHAsO_4 \cdot H_2O$) and barium arsenate ($Ba_3(AsO_4)_2$) were synthesized by adding 20 mL and 30 mL of 0.2 mol L^{-1} CO_2-free barium solution (from $BaCl_2 \cdot 2H_2O$) into a 20 mL of 0.2 mol L^{-1} of As(V) solution (from $As_2O_5 \cdot 12H_2O$) at pH 6 and 12 using 0.01 and 0.1 M NaOH (Zhu et al. 2005). After stabilization at room temperature for 1 h, white precipitates of the three standard materials were separated by filtration, washed with water and ethanol, dried in a vacuum drier at 40 °C overnight, and stored in a desiccator for further analysis.

Co-precipitation of As(V) with barite

The co-precipitation experiments were performed by titrating CO_2-free $BaCl_2 \cdot 2H_2O$ solution into the mixture of CO_2-free Na_2SO_4 solution and $As_2O_5 \cdot 12H_2O$ solution (Tokunaga et al., 2016). Briefly, 30 mL of 0.2 mol L^{-1} sulfate solution (pH 3, 4, 5, 6, 7, 8, 9, 10) and same pH 30 mL of As solution with different concentrations were mixed in a beaker, the pH was adjusted to the desired values (pH 3, 4, 5 6, 7, 8, 9, 10) using 0.01 and 0.1 M NaOH as a base, followed by addition of 30 mL of 0.2 mol L^{-1} barium solution (i.e. equimolar Ba^{2+} and SO_4^{2-} ions) with magnetic stirring. The mixtures were allowed to stabilize for 24 h with the pH controlled at a constant value. The As(V) concentration in the system (i.e. 50, 500, 2000 mg L^{-1}) based on the final volume is reported.

After stabilization, the solids were rinsed 5 times with DI water and separated by centrifugation, dried in a vacuum oven at 40 °C overnight, and stored in a desiccator at room temperature for further analysis.

To obtain the As(V)-doped barite, an aliquot of each As(V)-barite coprecipitate was repeatedly treated with 1 M H_2SO_4 solution for 5 times in order to remove $BaHAsO_4 \cdot H_2O$ and/or $Ba_3(AsO_4)_2$ phases that could precipitate during the co-precipitation process (Bluteau and Demopoulos 2007). This procedure was applied because barium arsenate phases are very soluble in acids. Then the acid treated solid was rinsed with DI water for 3 times and dried for further analysis. The acid-treated and non-acid treated coprecipitated samples are designated with a prefix AT and UT hereafter in the manuscript, respectively.

Determination of As concentrations in the solid phases

The As concentrations in the UT and AT samples were measured using XRF (Thermo Fisher Niton XL2) (Ene et al., 2010) equipped with X-ray source and an energy-resolving detector. The X-ray was produced by an X-ray source of Ag target run at a voltage of 40 kV with 80 μA current and the ray was collimated with slits collimators. The sample flat discs were prepared prior to XRF analyses, as suggested by the user manual (Thermo Fisher Niton XL2). The samples were placed on the sample stage to make sure that the investigated area of samples is in the optical focus (Jiang et al. 2015). Each sample was measured in triplicates and the mean value is reported. The detection limit of the instrument is approximately 10 $\mu g\ g^{-1}$. Standard solid reference material (CCRMP TILL-4, soil) was analyzed to assure the accuracy of the total As concentration. The measured As concentration of standard material was 107 ± 9.7 $\mu g\ g^{-1}$, which was highly consistent with the certified value of 111 $\mu g \cdot g^{-1}$.

126 **Geochemical modelling**

127 The Phreeplot software coupled with a batch version PHREEQC was employed
128 to calculate the equilibrium phases and speciation of As in the As(V)-Ba-SO_4
129 co-precipitation systems as a function of pH and initial As(V) concentrations
130 (Kinniburgh and Cooper 2011). The modelling was performed in a 0.1 M NaCl media
131 at 25 °C. The thermodynamic database of wateq4f supplied with the software was
132 modified to include the thermodynamic data of $BaHAsO_4 \cdot H_2O$ ($logK_{sp}$ = -5.6) and
133 $Ba_3(AsO_4)_2$ ($logK_{sp}$ = -23.53) (Zhu et al. 2005; Nordstrom et al. 2014).

134 **XRD characterization**

135 The mineralogical characteristics of the synthetic barite and the AT samples
136 precipitated at pH 4, 7, and 10 with the aqueous As concentration of 2000 mg L^{-1}
137 were characterized by using a Rigaku D/max 2400 X-ray diffractometer (Rigaku
138 Corporation, Japan) equipped with a copper target (Cu $K\alpha_1$ radiation, λ=1.5418Å), a
139 crystal graphite monochromator and a scintillation detector. The equipment was run at
140 56 kV and 182 mA by step scanning from 10° to 80° 2θ with increments of 0.02° 2θ.
141 For the refinements of the arsenate incorporated barite structures, the sulfur position
142 was assumed to be shared with the arsenic atom and the occupancy was calculated
143 from the concentration of arsenate in the AT samples.

144 **SEM characterization**

145 The morphologies of the solid samples were analyzed on a FEI Quanta 250
146 scanning electron microscope. The samples were mounted on pin stubs by use of
147 double-sided carbon tape and sputter-coated with gold, and imaged at 30 kV and a

148 magnification factor of 5000 and 20000.

149 **FTIR measurement**

150 The infrared spectra of the powdered samples were collected on a Thermo
151 Nicolet 6700 Fourier transform infrared spectrometer. The KBr sample discs were
152 prepared by mixing 0.5% of finely ground samples in high-purity KBr and pressed
153 using a hydraulic press. Then each sample was scanned 200 times in the mid-IR range
154 (400-4000 cm^{-1}) with a resolution of 4 cm^{-1} in transmission mode and the averaged
155 spectrum was reported.

156 **XAFS measurement and data processing**

157 The As *K*-edge XAFS spectra of the AT samples coprecipitated at the initial
158 As(V) concentration of 2000 mg L^{-1} and pH 3, 7, and 10 as well as the reference
159 materials ($BaHAsO_4 \cdot H_2O$ and $Ba_3(AsO_4)_2$) were collected on the XAFS beamline
160 (1W1B) at Beijing Synchrotron Radiation Facility (BSRF). To avoid As(V)
161 photoreduction under the beam, all spectra were recorded at 77 K using a homemade
162 cryostat (Mercier-Bion et al., 2011). The BSRF storage ring was run at 2.5 G eV in
163 full-energy injection mode and 250 mA beam current. The monochromator on
164 beamline was a fixed exit double crystal monochromator with Si (111) crystals. The
165 absolute position of the monochromator was calibrated by an Au L_3-edge spectrum.
166 The scan steps for the XANES and EXAFS regions were set to 0.7 eV and 3 eV,
167 respectively. The spectra of reference materials were collected in transmission mode
168 using an ionization chamber and the As(V)-doped barites were measured in
169 fluorescence mode.

Data normalization was performed by using Athena in the Demeter package (version 0.9.25) (Ravel and Newville 2005). The spectra were background subtracted and normalized to the atomic absorption. The pre-edge of all spectra was fitted with a straight line in the range of 150 – 50 eV before the absorption edge. The post-edge absorption background was subtracted by fitting a cubic polynomial spline to the data in the energy range of 150 – 750 eV after the absorption edge. The EXAFS spectra were Fourier transformed from k to R space using Kaiser-Bessel apodization windows with R_{bkg} value of 0.9 Å. The k-space range was set to 3 – 13.5 $Å^{-1}$ to obtain the radial structural functions (RSFs). Final fitting of the spectra was done on Fourier transformed k^3 weighted spectra in R space. For data fitting and modeling, scattering paths were calculated with ATOMS and FEFF using crystallographic data of $BaHAsO_4 \cdot H_2O$ (Jimenez et al. 2004), $Ba_3(AsO_4)_2$ (Park and Bluhm 1996) and DFT optimized structure as model structures.

DFT modeling

The structures of As(V)-doped barite (2×2×2 supercell) were optimized with DFT calculations using pw.x code available in QUANTUM ESPRESSO package (Version 6.0) (Giannozzi et al. 2009). The content of As(V) in the As-doped barite supercell is approximately 10 mg g^{-1}, which is comparable to the highest As content in the AT sample (~8.9 mg g^{-1}). The program uses plane waves and pseudopotentials to solve the Kohn-Sham equations. The geometric optimization was performed in a periodic system using the generalized gradient approximation, the Perdew–Burke–Ernzerhof (GGA-PBE) function (Giacomazzi and Scandolo 2010), and the

192 semi-empirical dispersion correction at D2 level (DFT-D2) (Grimme 2006). The
193 norm-conserving pseudopotentials were used for all calculations. Calculations for
194 supercells with dimension of 14.31×17.76×10.91 $Å^3$ (containing 193 atoms) were
195 carried out at the Γ-point of the Brillouin zone to save the computation cost, but for
196 bulk barite and $BaHAsO_4 \cdot H_2O$, denser k-mesh of 4 × 4 × 4 was used. The plane-wave
197 kinetic energy cut-off for wave functions (charge density and potential) was set to 80
198 Ry (320 Ry). Tests showed that these parameters could give satisfactory convergence
199 of total energy (< 0.2 mRy/atom).

200 **XANES analysis**

201 The XANES data in the range of -20 to 150 eV below and above the absorption
202 edge was analyzed by the full potential multiple scattering theory using the recently
203 developed FPMXAN code (Benfatto et al. 2001a, 2001b; Hayakawa et al. 2007;
204 Hatada et al. 2007, 2009, 2010), which has been used to investigate the local structure
205 of hydrous ferric arsenate and the detail method have been described elsewhere
206 (Wang et al. 2016). FPMXAN uses the full potential multiple scattering theory to
207 approximate the shape of the potential based on the local density approximation of the
208 self-energy of the excited photoelectron. The self-energy is calculated using the real
209 part of the Hedin-Lundqvist potential. The fitting quality was evaluated using the
210 square residue function (S^2) as following equation (Benfatto et al. 2001a, 2001b):

$$S^2 = n \frac{\sum_{i=1}^{m} \omega_i \left[\left(\chi_i^{th} - \chi_i^{exp} \right) \varepsilon_i^{-1} \right]^2}{\sum_{i=1}^{m} \omega_i} \quad (1)$$

211

212 where n represents the number of independent parameters, m: represents the number

213 of data points, y_i^{th} and y_i^{exp} represent the theoretical and experimental values,
214 respectively, ε_i is the error in each point of the experimental data set, and w_i is a
215 statistical weight.

216 **RESULTS AND DISCUSSION**

217 **As concentrations in the solid phases**

218 Arsenic content in the coprecipitated solids showed clear increasing tendency as
219 the pH values and the initial aqueous As concentrations increased (Fig. 1). The As(V)
220 contents in the UT samples increased with increasing pH and were in the range of
221 0.12 – 2.8 mg g^{-1}, 0.72 – 11.5 mg g^{-1}, and 2.3 – 20.2 mg g^{-1} for the initial aqueous
222 As(V) concentration of 50, 500, and 2000 mg L^{-1}, respectively. Accordingly, the
223 content of As(V) in the AT samples was in the range of 0.12 – 2.5 mg g^{-1}, 0.72 – 4.9
224 mg g^{-1}, and 2.28 – 8.9 mg g^{-1} increasing with pH. The content of As in the AT
225 samples were almost equal to those of corresponding UT samples at lower pH (i.e. pH
226 3 – 5) for each initial As(V) concentrations. This meant that As(V) was unable to be
227 extracted from the solids by 1 M H_2SO_4, indicating that the As(V) was dominantly
228 fixed by incorporation into the barite structure at pH 3 - 5. The increasing As content
229 in the AT samples from pH 3-10 indicated that more As(V) was incorporated into
230 barite structure at higher pH. It is worth to note that the acid treatment by 1 M H_2SO_4
231 resulted in a significant difference in As(V) concentrations in the UT and AT samples
232 at pH > 5. The latter fact meant that the formation of acid soluble phases during
233 co-precipitation occurred (Zhu et al. 2005; Weil 2016).

234 The saturation state with respect to barium (hydrogen) arsenate in the

As(V)-barite co-precipitation systems at different pH and initial arsenic concentrations were calculated (Zhu et al. 2005; Nordstrom et al. 2014). The results (Fig. 2) show that $BaHAsO_4 \cdot H_2O$ precipitates in weak acidic to neutral pH conditions while $Ba_3(AsO_4)_2$ precipitates at the pH greater than neutral conditions, in agreement with previous experimental and modelling work (Zhu et al. 2005). This suggests that the coprecipitated solids at weak acidic to neutral conditions were probably the mixtures of $BaSO_4$, $BaHAsO_4 \cdot H_2O$, and $Ba_3(AsO_4)_2$, while the coprecipitates formed at neutral to alkaline conditions likely contain both $BaSO_4$ and $Ba_3(AsO_4)_2$. Therefore, the UT samples could be mixtures of As(V)-doped barite and barium arsenate phases, while the AT samples represent only As(V)-doped barite because acid treatment removed the barium arsenate phases that could have formed during co-precipitation.

Morphology of the precipitated solids

The SEM images of the As(V)-barite coprecipitates formed at pH 6, 9 and 10 and the initial As(V) concentration of 2000 mg L^{-1} are compared with As(V)-free barite, $BaHAsO_4 \cdot H_2O$, and $Ba_3(AsO_4)_2$ standard materials in Figure 3. As(V)-free barite crystals occurred as rice-shaped particles, while $BaHAsO_4 \cdot H_2O$ and $Ba_3(AsO_4)_2$ appear as irregular plates and irregular particles, in agreement with previous works (Essington, 1988; Zhu et al., 2005). Compared with As(V)-free barite and $BaHAsO_4 \cdot H_2O$, the morphologies of UT and AT As(V)-barite coprecipitates were remarkably modified (Fig. 2D-I). The morphology of the pH 6 UT and AT samples changed to spherical particles as well as some irregular plates. At pH 9 and 10, the morphologies of the UT and AT precipitates appeared to be the aggregation of small

particles and the particle size significantly decreased (Fig. 3E, F, H, I). The aggregation of small particles and decrease in particle size maybe due to the hindering effect of the formation of $BaHAsO_4 \cdot H_2O$ and/or $Ba_3(AsO_4)_2$ phases and the higher amount of As(V) incorporated into barite structure which inhibits the growth of barite particles.

Mineralogical results

The mineralogical characteristics of the AT As(V)-barite coprecipitates synthesized at initial As(V) concentration of 2000 mg L^{-1} and pH 4, 7, and 10 were analyzed by XRD (Fig. 4). Barite was the only XRD identifiable crystalline phase in all samples (Jacobsen 1998; Hartman and Strom 1989) and no identifiable diffraction lines of crystalline $BaHAsO_4 \cdot H_2O$ and $Ba_3(AsO_4)_2$ were observed. Incorporation of As(V) slightly altered the X-ray diffraction features of barite. In the case of the As(V)-free barite, the strongest diffraction peak was the (210) plane located at ~26°, but in the As(V) incorporated samples, the strongest diffraction peak shifted to the (211) plane located at ~28°. This effect may be ascribed to the change in the preferred orientation induced by the incorporation of As(V). The Rietveld refinements showed that the incorporation of As(V) into the structure of barite induced the volume expansion of its unit cell (Table S3), possibly resulting from the larger size of AsO_4 tetrahedron than SO_4.

FTIR spectroscopy

The UT and AT samples were characterized using FTIR spectroscopy (Fig. 5). Since barite does not contain water molecules, only the frequency region of interest

(400-1300 cm^{-1}) is displayed where the stretching and bending vibrations of As-O and S-O bonds show characteristic infrared active bands (Omori 1968; Myneni et al. 1998; Jia et al. 2007).

The As(V)-free barite showed typical bands of the v_1(A1), v_2(E), v_3(F2) and v_4(F2) at 938, 418, [1074, 1110, 1203], and [609, 642] cm^{-1} (Fig. 5), in agreement with reference literature (Omori 1968). The FTIR spectrum of $Ba_3(AsO_4)_2$ shows a very broad band peaking at 813 cm^{-1}, which was reasonably assigned to a combination of v_3 (F2) and v_1 (A1) arsenate ions. In the case of $BaHAsO_4 \cdot H_2O$, the weak band at 692 cm^{-1} was attributed to the v_s of the As-OH bond and the strong bands at 860 and 877 cm^{-1} arose from the v_s and v_{as} of the As-O bond in the $HAsO_4^{2-}$ group.

All the As(V)-free barite and As(V)-barite coprecipitates showed the S-O stretching and bending vibrations at nearly the same frequencies (Fig. 5A). Moreover, the degeneracy of the SO_4 vibrational modes does not change from the As(V)-free barite to the As(V) coprecipitates, indicating that the majority of the symmetry and bonding environment in the SO_4 groups of the barite structure remains almost unchanged due to the low concentration of As(V) incorporated into the barite structure (< 1.0 wt. %). The weak band at 982 cm^{-1} and three strong bands at 1000 – 1300 cm^{-1} on the FTIR spectra were assigned to the v_1 symmetric and the v_3 antisymmetric stretching vibration of SO_4^{2-}. The v_2 symmetric and v_4 antisymmetric bending of SO_4^{2-} tetrahedral appeared at 418 and [609, 640] cm^{-1}, respectively (Omori 1968; Shen et al. 2007; Bahl et al. 2014).

Some small features emerged in the range of 700 – 900 cm^{-1} on the FTIR spectra of the As(V)-barite coprecipitates (Fig. 5B) which are attributed to the As-O stretching vibrations. Because the UT coprecipitated samples could contain various arsenate species (i.e. As(V)-doped barite, $BaHAsO_4 \cdot H_2O$ and $Ba_3(AsO_4)_2$), the As-O stretching vibration bands are likely composites of the arsenate vibrational modes from these phases. The FTIR spectra of UT-pH 7 and 9 samples showed broad bands overlapped with four to five bands at 814, 837, 854, 878, and 892 cm^{-1}. The band at 814 cm^{-1} on the UT-pH 9 spectrum disappeared after acid treatment (AT-pH 9) to remove barium arsenate phases. Hence the band at 814 cm^{-1} coincides with the broad band observed in $Ba_3(AsO_4)_2$, which is estimated to be the barium arsenate phase at pH 9 based on the geochemical modelling (Fig. 2). These results are in agreement with previous studies, Rodríguez-Blanco et al (2007, 2008) states that at pH 7 the dominant As species is $HAsO_4^{2-}$ and the arsenate precipitating is pharmacolite ($CaHAsO_4 \cdot H_2O$) and two As species ($HAsO_4^{2-}$ and AsO_4^{3-}) are incorporated in the crystal structure of precipitates obtained at pH 9. The FTIR spectrum of the UT-pH 5 sample does not show the 814 cm^{-1} band of $Ba_3(AsO_4)_2$, in agreement with the geochemical modelling results that $Ba_3(AsO_4)_2$ phase is less likely to form at pH < 6.

The FTIR spectra of acid-treated coprecipitate samples displayed three As-O stretching vibration bands at 892, 878 and 854 cm^{-1} with the band intensity increasing with pH, which is consistent with the relative contents of arsenic in the AT samples. The FTIR spectra of all AT samples also showed very weak bands at 837 and 708 cm^{-1} due to the very low arsenic content. Because the AT samples were treated with

an acid repeatedly to remove the $BaHAsO_4 \cdot H_2O$ and/or $Ba_3(AsO_4)_2$ phases that may have formed, these FTIR bands can be attributed to the As(V) incorporated into barite. The weak band at 708 cm^{-1} is attributed to As-OH stretching vibration (Myneni et al. 1998). Therefore, the arsenate species incorporated into barite structure is most likely $HAsO_4^{2-}$.

EXAFS analysis

The EXAFS data of the AT samples as well as our standard $BaHAsO_4 \cdot H_2O$ and $Ba_3(AsO_4)_2$ were fitted using the crystallographic data of $Ba_3(AsO_4)_2$ (Park and Bluhm 1996), $BaHAsO_4 \cdot H_2O$ (Jimenez et al. 2004) and DFT optimized structure as the initial models for comparison (Fig. S1 and Table 1).

In the case of the standard $BaHAsO_4 \cdot H_2O$, the EXAFS fitting gave an As-O and As-OH bonds with an interatomic distance of 1.68 Å with CN of 3 and 1.76 with CN of 1 for first shell, an As-Ba interatomic distance of 3.6-4.2 Å for second shell with CN of 5 shell, in agreement with reported crystallographic data (Park and Bluhm 1996). For the standard $Ba_3(AsO_4)_2$, an As-O bond at 1.70 Å with a CN of 4 for first shell and an As-Ba interatomic distance of 3.4-3.8 Å for second shell with CN of 6 was determined, again in agreement with previous published crystallographic data (Jimenez et al. 2004). For the AT samples at the three selected pH conditions, the EXAFS fitting using $BaHAsO_4 \cdot H_2O$ model for first shell ($R+\Delta R$ = 0.9 – 2.0 Å) showed that the first-neighbor contributions were fitted with 3 oxygen (O) atoms at 1.67 Å from As-O and 1 O atom at approximately 1.75 Å from As-OH, with an average of 1.69 Å (Fig. 6 and Table 1). The second shell ($R+\Delta R$ = 2.0 – 3.8 Å) was

used the DFT optimized structure (Fig S1) as the initial model. The crystallographic data of DFT optimized structure as the initial model fitted the EXAFS data with 6 As-Ba paths at an interatomic distance of approximately 3.5-3.8 Å with CN of 6 (Table 1). In the case of crystallographic data of $Ba_3(AsO_4)_2$ as the initial model fitted the EXAFS data showed 4 As-O paths at an interatomic distance of approximately 1.69 Å (Table S4). The second shell (2.0-3.6 Å) gave an As-Ba interatomic distance of 3.0-3.6 Å with CN of 4 when used the DFT optimized structure as the initial model (Table S4). The comparison between two models ($BaHAsO_4 \cdot H_2O$ and $Ba_3(AsO_4)_2$/+DFT optimized structure) showed that the $BaHAsO_4 \cdot H_2O$ resulted in smaller goodness-of-fit, the *R*-factor and reduced χ^2 in comparison to the $Ba_3(AsO_4)_2$ model for all AT samples. This may imply that the $BaHAsO_4 \cdot H_2O$ produced a better fit than the $Ba_3(AsO_4)_2$ model, possibly due to the fact that the As(V) species incorporated into the barite structure was more likely in the form of $HAsO_4^{2-}$, in agreement with FTIR results.

DFT and XANES analysis

The FTIR and EXAFS results showed that $HAsO_4^{2-}$ is more likely to be dominant species in barite structure. However, FTIR spectroscopy and EXAFS analysis can not give the detail local structure of $HAsO_4^{2-}$. Since the oscillation in the near edge part (XANES) of XAFS spectra is much stronger than that in the extended part (EXAFS), XANES features are more sensitive to the atomic positions and have been used to probe the interatomic distances and angles based on the muffin-tin approximation (Benfatto et al. 2001a, 2001b; Hayakawa et al. 2007) and FPMS

367 method (Hatada et al. 2007, 2009, 2010). Therefore, we used DFT calculation to
368 construct the initial model and refined the local structure using FPMS theory.

369 The DFT optimized local structure are shown in Figure S1 and Table S5. The
370 optimized S-O bond lengths were averaged at 1.48 ± 0.011 Å for As(V)-doped
371 configuration, in good agreement with the As-free barite (1.48 ± 0.011 Å) and the
372 crystallographic data (1.48 ± 0.017 Å) reported by Jacobsen et al. (1998) (Jacobsen et
373 al. 1998), implying that the influence of the incorporation of small amount of As(V)
374 in barite structure on SO_4 groups was very limited. The As-O bond lengths were 1.660,
375 1.651, and 1.663 Å, with the As-OH bond length of 1.766 Å.

376 All As *K*-edge XANES spectra of the As(V)-doped barite samples showed a well
377 resolved near edge white line peak at an energy of 11,875.0 eV which was similar to
378 that of the reference materials ($BaHAsO_4 \cdot H_2O$ and $Ba_2(AsO_4)_3$) indicating that the As
379 incorporated into the barite structure occurred as As(V). The difference among the
380 XANES spectra of the AT samples precipitated at different pH values was negligible
381 except minor difference near the energy position of the white line peak (Fig. 7B). This
382 meant that the As(V) incorporated into the barite structure of our As(V) coprecipitates
383 had a similar electronic environment and geometric structure.

384 In order to probe the local structure of As(V) incorporated into barite lattice, *ab*
385 *initio* FPMS simulations of XANES spectra were performed. The As *K*-edge XANES
386 spectra of the AT sample precipitated at pH 7 was used as a representative due to high
387 similarity among different AT samples (Fig. 7B). The DFT optimized structure as the
388 initial model (cluster radius = 6 Å and 67 atoms) was used to calculate the theoretical

389 XANES spectrum. The comparison between unbroadened theoretical and
390 experimental spectra showed that all the XANES features have been reproduced (Fig.
391 7C). After refinement of the non-structural parameters, a satisfactory goodness of fit
392 (S^2 = 2.9) was obtained. This result indicated that the species of As(V) incorporated in
393 barite mainly occurred as $HAsO_4^{2-}$, consistent with our FTIR and EXAFS results.
394 Then the interatomic distances and angles in the DFT model were refined
395 shell-by-shell to probe the local structure of $HAsO_4^{2-}$ in the barite structure. During
396 the structural refinement, the SO_4^{2-} ions were regarded as groups and moved together.
397 The refinement gave good consistency between the theoretical XANES spectra and
398 the experimental data with a goodness of fit of S^2 = 1.6 (Fig. 7D). From the
399 refinement, it was determined that the bond lengths of As-O/H in the arsenate
400 tetrahedral were 1.63, 1.64, 1.68, and 1.75 Å with an average of 1.68 ± 0.05 Å (Fig.
401 7E), in good agreement with the EXAFS and DFT results.
402
403 **SUMMARY**
404 The species of As(V) in solid phase during the co-precipitation of As(V), Ba, and
405 SO_4^{2-} at various pH's (3 – 10) and initial aqueous As(V) concentrations (50, 500 and
406 2000 mg L^{-1}) was investigated in this work. The As(V) in the coprecipitates was
407 dominantly present as incorporated species in the barite structure at pH ≤ 5, while at
408 higher pH, $BaHAsO_4 \cdot H_2O/Ba_2(AsO_4)_3$ could form under our experimental conditions.
409 The content of As(V) incorporated in the barite lattice increased up to 8.9 mg g^{-1} (0.89
410 wt. %) as the pH and initial As(V) concentration increased. FTIR, DFT, and XAFS

411 data suggested that the As species in the crystal lattice of barite was dominantly
412 presented as $HAsO_4^{2-}$. The FPMS structural refinement delivered the As-O
413 interatomic distance of 1.63, 1.64, 1.68, and 1.75 Å with an average of 1.68 ± 0.05 Å,
414 in good agreement with the EXAFS and DFT results.

415 The previous studies have stated that the arsenite molecule (AsO_3^{3-}) substituted
416 by CO_3^{2-} in the calcite structure results in a nonbalanced local charge (Benedetto et al.,
417 2006). In the same way, other authors hypothesize that the charge balance of uranyl
418 ions incorporated in calcite through a nonlocal mechanism by which Na^+ cation would
419 be compensating the charge (Kelly et al., 2003). Our results suggested that the As(V)
420 species in the crystal lattice of barite was dominantly presented as $HAsO_4^{2-}$, having
421 same charge with SO_4^{2-}, via a solid solution mechanism. Hence, charge balance is a
422 strict requirement for the As(V) substitution of SO_4 that may occur in ion exchange
423 processes.

424 **IMPLICATIONS**

425 Incorporation of arsenate into mineral lattices (e.g. vivianite, rhomboclase,
426 hematite, gypsum, hydroxylapatite, jarosite) (Fernández-Martínez et al. 2008; Lee et
427 al. 2009; Kendall et al. 2013; Bolanz et al. 2013, 2016; Muehe et al. 2016) is an
428 important process influencing the mobility and transformation processes of arsenate in
429 nature and mining related environments. In hot spring water (Tokunaga et al. 2016),
430 some mining related areas and other geological environments (e.g. deep-sea,
431 groundwater, river, and crust deposits) (Goodarzi 2002; McBeth et al. 2003; Pone et
432 al. 2007; Arik and Sgem 2008; Romero et al. 2010; Liu and Hendry 2011; Gomez et

433 al. 2013) that contain considerable amounts of As, it can co-exist with Ba^{2+} and SO_4^{2-}
434 leading to the formation of arsenate-barite. The structural incorporation of arsenate
435 into barite represents a sink for arsenic that can impact its mobility and transformation
436 in the environment. To date, there exists limited examples in the literature (Goodarzi
437 2002; McBeth et al. 2003; Pone et al. 2007; Arik and Sgem 2008; Romero et al. 2010;
438 Tokunaga et al. 2016) on the incorporation of arsenate into barite, how it affects
439 arsenic mobility and transformation in the environment. Moreover, the state of
440 arsenate (protonated or not) incorporated into the barite structure is definitively not
441 well understood, this latter fact is important to know as it may affect some of the
442 chemical properties of the arsenate incorporated barite such as arsenic stability as seen
443 for other mining-geological related phases (Gomez et al. 2011). For example,
444 Tokunaga et al (2006) focused on the influence of As oxidation state in natural barite
445 and its immobilization as well as the ratio of As(III)/As(V) as an indicator for
446 sub-oxic/anoxic redox conditions. In this work, the authors did not consider the
447 coprecipitation of arsenate with barium at neutral conditions, how this may lead to
448 multiple arsenate species, the amount of arsenate in the barite lattice as a function of
449 pH and the arsenate speciation in the barite structure. In the present work, we studied
450 the amount of arsenate in barite, the possible barium arsenate phases, the dominant
451 arsenate species in the barite structure and local atomic structure of As(V) in the
452 barite crystal lattice formed at various pH. The latter facts are of significance for
453 understanding the speciation and formation of Ba^{2+}, SO_4^{2-} minerals in the presence of
454 arsenate as well as the aqueous arsenic fixation and mobility in some natural and

455 mining-impacted environments with Ba^{2+} and SO_4^{2-}. In natural systems, the presence
456 of CO_3^{2-} may induce the formation of $BaCO_3$ (i.e. witherite, $\log K_{sp}$ = -8.562), which
457 may also incorporate arsenic. However, $BaCO_3$ will transform to barite in the
458 presence of SO_4^{2-} due to its relatively higher solubility. Therefore, our findings can
459 reflect the effect of barite precipitation on the mobility of As in natural environment.

460

461 **ACKNOWLEDGMENTS**

462 The staff of the XAFS beamline at the Beijing Synchrotron Radiation Facility are
463 appreciated for their help on the As *K*-edge XAS spectral measurements. This work
464 was financially supported by the National Natural Science Foundation of China (No.
465 41530643), the Strategic Priority Research Program of the Chinese Academy of
466 Sciences (No. XDB14020203) and the National Natural Science Foundation of China
467 (Nos. 41473111, 41303088, and 41373127).

468

REFERENCES

Acharyya, S.K., Chakraborty, P., Lahiri, S., Raymahashay, B.C., Guha, S., and Bhowmik, A. (1999) Arsenic poisoning in the Ganges delta. Nature, 401, 545-545.

Arik, F. (2008) Geology, mineralogy and geochemical characteristics of the gozecukuru (kutahya) As-Sb deposits, NW TURKIYE. Sofia: Int Scientific Conference Sgem, 91-98.

Bahl, S., Lochab, S.P., Pandey, A., Kumar, V., Aleynikov, V.E., Molokanov A.G., and Kumar, P. (2014) Characterization and luminescence studies of Eu doped Barite nanophosphor. Journal of Luminescence, 149, 176-184.

Benfatto, M., and Della, L.S. (2001a) Geometrical fitting of experimental XANES spectra by a full multiple-scattering procedure. Journal of Synchrotron Radiation, 8, 1087-1094.

Benfatto, M., Congiu-Castellano, A., Daniele, A., and Longa, S.D. (2001b) MXAN: a new software procedure to perform geometrical fitting of experimental XANES spectra. Journal of Synchrotron Radiation, 8, 267-269.

Bluteau, M.C., and Demopoulos, G.P. (2007) The incongruent dissolution of scorodite - Solubility, kinetics and mechanism. Hydrometallurgy, 87, 163-177.

Bolanz, R.M., Wierzbicka-Wieczorek, M., Caplovicova, M., Uhlik, P., Gottlicher, J., Steininger, R., and Majzlan, J. (2013) Structural Incorporation of As^{5+} into Hematite. Environmental Science & Technology, 47, 9140-9147.

Bolanz, R.M, Gottlicher, J., Steininger, R., and Wieczorek, A. (2016) Structural

incorporation of As^{5+} into rhomboclase ((H_5O_2) $Fe^{3+}(SO_4)_{(2)}$center dot $2H_{(2)}O$) and $(H_3O)Fe(SO_4)_{(2)}$. Chemosphere, 146, 338-345.

Das, D., Samanta G., Mandal, B.K., Chowdhury, T.R., Chanda, C.R., Chowdhury, P.P., Basu, G.K., and Chakraborti, D. (1996) Arsenic in groundwater in six districts of West Bengal, India. Environmental Geochemistry and Health, 18, 5-15.

Dutrizac, J.E., and Jambor, J.L. (2007) Characterization of the iron arsenate–sulphate compounds precipitated at elevated temperatures. Hydrometallurgy, 86, 147-163.

Benedetto, F., Costagliola, P., Benvenuti, M., Lattanzi, P., Romanelli, M., and Tanelli, G. (2006) Arsenic incorporation in natural calcite lattice: Evidence from Electron Spin Echo spectroscopy. Earth and Planetary Science Letters, 246, 458-465.

Ene, A., Bosneaga, A., and Georgescu, L. (2010) Determination of heavy metals in soils using XRF technique. Romanian Journal of Physics, 55, 815-820.

Fernández-Martínez, A., Cuello, G.J., Johnson, M.R., Bardelli, F., Roman, R.G., Charlet L., and Turrillas X. (2008) Arsenate incorporation in gypsum probed by neutron, X-ray scattering and density functional theory modeling. Journal of Physical Chemistry A, 112, 5159-5166.

Giacomazzi, L., and Scandolo, S. (2010) Gypsum under pressure: A first-principles study. Physical Review B, 81.

Giannozzi, P., Baroni, S., Bonini, N., Calandra, M., Car, R., Cavazzoni, C., Ceresoli,

513 D., Chiarotti, G.L., Cococcioni, M., Dabo, I., and others. (2009) QUANTUM
514 ESPRESSO: a modular and open-source software project for quantum
515 simulations of materials. Journal of Physics-Condensed Matter, 21, 395502.
516 Giere, R., Sidenko, N.V., and Lazareva, E.V. (2003) The role of secondary minerals
517 in controlling the migration of arsenic and metals from high-sulfide wastes
518 (Berikul gold mine, Siberia). Applied Geochemistry, 18, 1347-1359.
519 Gomez, M.A., Assaaoudi, H., Becze, L., Cutler, J.N., and Demopoulos, G.P. (2010)
520 Vibrational spectroscopy study of hydrothermally produced scorodite
521 ($FeAsO_4$•$2H_2O$), ferric arsenate sub-hydrate (FAsH; $FeAsO_4$•$0.75H_2O$) and
522 basic ferric arsenate sulfate (BFAS; Fe $(AsO_4)_{(1-x)}(SO_4)_{(x)}(OH)_{(x)}$•$wH_2O$).
523 Journal of Raman Spectroscopy, 41, 212-221.
524 Gomez, M.A., Becze, L., Cutler, J.N., and Demopoulos, G.P. (2011) Hydrothermal
525 reaction chemistry and characterization of ferric arsenate phases precipitated
526 from $Fe_2(SO_4)_3$-As_2O_5-H_2SO_4 solutions. Hydrometallurgy, 107, 74-90.
527 Gomez, M.A., Hendry, M.J., Koshinsky, J., Essilfie, D.J., Paikaray S., and Chen J.
528 (2013a) Mineralogical Controls on Aluminum and Magnesium in Uranium
529 Mill Tailings: Key Lake, Saskatchewan, Canada. Environmental Science &
530 Technology, 47, 7883-7891.
531 Gomez, M.A., Ventruti, G., Celikin, M., Assaaoudi, H., Putz, H., Becze, L., Lee, K.E.,
532 and Demopoulos, G.P. (2013b) The nature of synthetic basic ferric arsenate
533 sulfate ($Fe(AsO_4)_{(1-x)}(SO_4)_{(x)}(OH)_{(x)}$) and basic ferric sulfate ($FeOHSO_4$): their
534 crystallographic, molecular and electronic structure with applications in the

environment and energy. Rsc Advances, 3, 16840-16849.

Goodarzi, F. (2002) Mineralogy, elemental composition and modes of occurrence of elements in Canadian feed-coals. Fuel, 81, 1199-1213.

Grimme, S. (2006) Semiempirical GGA-type density functional constructed with a long-range dispersion correction. Journal of Computational Chemistry, 27, 1787-1799.

Hartman, P., and Strom, C.S. (1989) Structural morphology of crystals with the barite ($BaSO_4$) structure: A revision and extension. Journal of Crystal Growth, 502-512.

Hatada, K., Hayakawa, K., Benfatto, M., and Natoli, C.R. (2010) Full-potential multiple scattering theory with space-filling cells for bound and continuum states. Journal of Physics-Condensed Matter, 22, 185501.

Hatada, K., Hayakawa, K., Benfatto, M., and Natoli, C.R. (2007) Full-potential multiple scattering for x-ray spectroscopies. Physical Review B, 76, 060102.

Hatada, K., Hayakawa, K., Benfatto, M., and Natoli, C.R. (2009) Full-potential multiple scattering for core electron spectroscopies. Journal of Physics-Condensed Matter, 21, 104206.

Hayakawa, K., Hatada,, K., Della, L.S., D'Angelo, P., and Benfatto, M. (2007) Progresses in the MXAN fitting procedure. X-Ray Absorption Fine Structure-XAFS13, 882, 111-113.

Jacobsen, S.D., Smyth, J.R., Swope, R.J., and Downs, R.T. (1998) Rigid-body character of the SO4 groups in celestine, anglesite and barite, Can Mineral, 36,

1053-1060.

Jia, Y.F., Xu, L.Y., Wang, X., and Demopoulos, G.P. (2007) Infrared spectroscopic and X-ray diffraction characterization of the nature of adsorbed arsenate on ferrihydrite. Geochimica et Cosmochimica Acta, 71, 1643-1654.

Jiang, T.J., Guo, Z., Liu, J.H., and Huang, X.J. (2015) Electroadsorption-Assisted Direct Determination of Trace Arsenic without Interference Using Transmission X-ray Fluorescence Spectroscopy. Analytical Chemistry, 87, 8503-8509.

Jimenez, A., Prieto, M., Salvado, M.A., and Garcia-Granda, S. (2004) Structure and crystallization behavior of the (Ba,Sr)$HAsO_4$ center dot H_2O solid-solution in aqueous environments. American Mineralogist, 89: 601-609.

Kendall, M.R., Madden, A.S., Elwood Madden, M.E., and Hu, Q. (2013) Effects of arsenic incorporation on jarosite dissolution rates and reaction products. Geochimica et Cosmochimica Acta, 112, 192-207.

Kinniburgh, D.G., and Cooper, D.M. (2011) PhreePlot: creating graphical output with PHREEQC., Earth Sciences.

Kelly, S.D., Newville, M.G., Cheng, L., Kemner, K.M., Sutton, S.R., Fenter, P., Sturchio, N.C., Spötl‖, C. (2003) Uranyl Incorporation in Natural Calcite. Environmental Science & Technology, 37, 1284-1287.

Lee, J.U., Lee, S.W., Chon, H.T., Kim, K.W., and Lee, J.S. (2009) Enhancement of arsenic mobility by indigenous bacteria from mine tailings as response to organic supply. Environment International, 35, 496-501.

579 Lin, J.R., Chen, N., Nilges, M.J., and Pan, Y.M. (2013a) Arsenic speciation in
580 synthetic gypsum ($CaSO_4$•$2H_2O$): A synchrotron XAS, single-crystal EPR,
581 and pulsed ENDOR study. Geochimica et Cosmochimica Acta, 106, 524-540.
582 Lin, J.R., Chen, N., and Pan, Y.M. (2013b) Arsenic Incorporation in Synthetic
583 Struvite (NH_4MgPO_4•$6H_2O$): A Synchrotron XAS and Single-Crystal EPR
584 Study. Environmental Science & Technology, 47, 12728-12735.
585 Liu, D.J., and Hendry, M.J. (2011) Controls on (226)Ra during raffinate neutralization
586 at the Key Lake uranium mill, Saskatchewan, Canada. Applied Geochemistry,
587 26, 2113-2120.
588 McBeth, I., Reddy, K.J., and Skinner, Q.D. (2003) Chemistry of trace elements in
589 coalbed methane product water. Water Research, 37, 884-890.
590 Mercier-Bion, F., Drot, R., Ehrhardt, J.J., Lambert, J., Roques, J., and Simoni, E.
591 (2011) X-ray photoreduction of U(VI)-bearing compounds. Surface and
592 Interface Analysis, 43, 777-783.
593 Muehe, E.M., Morin, G., Scheer, L., Le, P.P., Esteve, I., Daus, B., and Kappler, A.
594 (2016) Arsenic(V) Incorporation in Vivianite during Microbial Reduction of
595 Arsenic(V)-Bearing Biogenic Fe(III) (Oxyhydr)oxides. Environmental
596 Science & Technology, 50, 2281-2291.
597 Myneni, S.C.B., Traina, S.J., Waychunas, G.A., and Logan, T.J. (1998) Vibrational
598 spectroscopy of functional group chemistry and arsenate coordination in
599 ettringite. Geochimica Et Cosmochimica Acta, 62, 3499-3514.
600 Nickson, R., McArthur, J., Burgess, W., Ahmed, K.M., Ravenscroft, P., and Rahman,

M. (1998) Arsenic poisoning of Bangladesh groundwater. Nature, 395, 338-338.

Nordstrom, D.K., Majzlan, J., and Konigsberger, E. (2014) Thermodynamic Properties for Arsenic Minerals and Aqueous Species. Reviews in Mineralogy and Geochemistry, 79, 217-255.

Omori, K. (1968) Infrared diffraction and the far infrared spectra of anhydrous sulfates. Mineralogical Journal, 5, 334-354.

Park, C.H., and Bluhm, K. (1996) Synthesis and crystal structure of barium boroarsenate $Ba(BAsO_5)$ with a contribution on barium orthoarsenate $Ba_3(AsO_4)_2$. Zeitschrift Fur Naturforschung Section B-a Journal of Chemical Sciences, 51, 722-726.

Pone, J.D.N., Hein, K.A.A., Stracher, G.B., Annegarn, H.J., Finkleman, R.B., Blake, D.R., McCormack, J.K., and Schroeder, P. (2007) The spontaneous combustion of coal and its by-products in the Witbank and Sasolburg coalfields of South Africa. International Journal of Coal Geology, 72, 124-140.

Ravel, B., and Newville, M. (2005) Athena, Artemis, Hephaestus: data analysis for X-ray absorption spectroscopy using IFEFFIT. Journal of Synchrotron Radiation, 12, 537-541.

Romero, F.M., Prol-Ledesma, R.M., Canet, C., Alvares, L.N., and Perez-Vazquez R. (2010) Acid drainage at the inactive Santa Lucia mine, western Cuba: Natural attenuation of arsenic, barium and lead, and geochemical behavior of rare

623 earth elements. Applied Geochemistry, 25, 716-727.

624 Rodríguez-Blanco., Jiménez, J.D., Prieto, A., and Torre, M. (2007) Oriented
625 overgrowth of pharmacolite on gypsum. Crystal Growth and Design, 7,
626 2756–2763.

627 Rodríguez-Blanco., Jiménez, J.D., Prieto, A., Torre, M., and García-Granda, L.,
628 Santiago. (2008) "Interaction of gypsum with As(V)-bearing aqueous
629 solutions: Surface precipitation of guerinite, sainfeldite, and
630 $Ca_2NaH(AsO_4)_2 \cdot 6H_2O$, a synthetic arsenate. American Mineralogist, 93,
631 928–939.

632 Savage, K.S., Bird, D.K., and O'Day, P.A. (2005) Arsenic speciation in synthetic
633 jarosite. Chemical Geology, 215, 473-498.

634 Shen, Y., Li, C., Zhu, X., Xie, A., Qiu, L., and Zhu J. (2007) Study on the preparation
635 and formation mechanism of barium sulphate nanoparticles modified by
636 different organic acids. Journal of Chemical Sciences, 119, 319-324.

637 Sherman, D.M., and Randall, S.R. (2003) Surface complexation of arsenic(V) to
638 iron(III) (hydr)oxides: structural mechanism from ab initio molecular
639 geometries and EXAFS spectroscopy. Geochimica et Cosmochimica Acta, 67,
640 4223-4230.

641 Sunyer, A., Currubí, M., and Viñals, J. (2013) Arsenic immobilization as alunite-type
642 phases: The arsenate substitution in alunite and hydronium alunite. Journal of
643 Hazardous Materials, 261, 559-569.

644 Tokunaga, K., Uruga, T., Nitta, K., Terada, Y., Sekizawa O., Kawagucci, S., and

645 Takahashi, Y. (2016) Application of arsenic in barite as a redox indicator for
646 suboxic/anoxic redox condition. Chemical Geology, in press.
647 Villanueva-Estrada, R.E., Prol-Ledesma, R.M., Rodriguez-Diaz, A.A., Canet C., and
648 Armienta, M.A. (2013) Arsenic in hot springs of Bahia Concepcion, Baja
649 California Peninsula, Mexico. Chemical Geology, 348, 27-36.
650 Wang, S., Ma X., Zhang, G., Jia, Y., and Hatada, K. (2016) New Insight into the
651 Local Structure of Hydrous Ferric Arsenate Using Full-Potential Multiple
652 Scattering Analysis, Density Functional Theory Calculations, and Vibrational
653 Spectroscopy. Environmental Science & Technology, 50, 12114–12121.
654 Weil, M. (2016) Insights into Formation Conditions, Crystal Structures, and Thermal
655 Behavior of Hydrous and Anhydrous Barium Arsenates. Crystal Growth &
656 Design, 16, 908-921.
657 Zhang, D., Yuan, Z., Wang, S., Jia, Y., and Demopoulos, G.P. (2015) Incorporation of
658 arsenic into gypsum:Relevant to arsenic removaland immobilization process in
659 hydrometallurgical industry. Journal of Hazardous Material, 300, 272-280.
660 Zhu, Y.N., Zhang, X.H., Xie, Q.L., Chen, Y.D., Wang, D.Q., Liang, Y.P., and Lu, J.
661 (2005) Solubility and stability of barium arsenate and barium hydrogen
662 arsenate at 25 degrees C. Journal of Hazardous Materials, 120, 37-44.
663
664
665
666

669 **LIST OF FIGURE CAPTIONS**

670 **FIGURE 1.** As content in the UT (solid symbol) and AT (open symbol) As(V)-barite
671 coprecipitates as a function of precipitation pH and initial As(V) concentrations (50,
672 500, 2000 $mg \cdot L^{-1}$). AT and UT mean acid treated and untreated samples, respectively.
673 The error bar represents one standard deviation of three individual experiments.

674

675 **FIGURE 2.** Geochemical modeling of the saturation states with respect to barium
676 arsenate in the As(V)-barite co-precipitation systems at pH 2-12 and initial arsenate
677 concentrations of 50 (●), 500 (○), 2000 (■) mg L^{-1}, respectively.

678

679 **FIGURE 3. SEM images of As(V)-free barite (A), $BaHAsO_4 \cdot H_2O$ (B), $Ba_3(AsO_4)_2$**
680 **(C), and As(V)-barite coprecipitates formed at pH 6, pH 9, pH 10 and an initial**
681 **As(V) concentration of 2000 mg L^{-1} with (D-F) and without (G-I) acid treatment.**

682

683 **FIGURE 4.** XRD patterns of the AT As(V)-barite coprecipitates formed at pH 4, 7,
684 10 and an initial As(V) concentration of 2000 mg L^{-1}. Black points and red lines
685 represent the experimental data and the Rietveld best fits, respectively.

686

687 **FIGURE 5.** FTIR spectra of the As(V)-free barite, $Ba_3(AsO_4)_2$, $BaHAsO_4 \cdot H_2O$
688 standards and the AT and UT As(V)-barite coprecipitates formed at various pHs (pH
689 3, 5, 7, and 9) and an initial As(V) concentration of 2000 mg L^{-1}.

690

691 **FIGURE 6.** The k^3-weighted χ functions (A), Fourier transformed (FTs)χ functions
692 (B), and real part of Fourier transformed EXAFS spectra (C) of the reference
693 materials and the As(V) doped-barite samples at pH 3, 7, and 10 with initial arsenate
694 concentration 2000 mg·L^{-1}: The $BaHAsO_4 \cdot H_2O$ (for first shell 0.9 - 2.0 Å) and DFT
695 optimized structure (Fig. S1) (for second shell 2 – 3.9 Å) were used as the model for
696 EXAFS fitting of the AT samples. The black dots and red lines represent the
697 experimental data and the best fits, respectively.
698
699 **FIGURE 7.** (A) Normalized As *K*-edge XANES spectra of reference materials
700 ($BaHAsO_4 \cdot H_2O$ and $Ba_3(AsO_4)_2$) and AT As(V)-barite coprecipitated at pH 3, 7, 10,
701 respectively. (B) The difference of XANES spectra among AT-pH3, AT-pH7, and
702 AT-pH10 samples. (C) Comparison between experimental As *K*-edge XANES spectra
703 of the AT-pH 7 sample (black circle-line), unbroadened (dash line), and broadened
704 theoretical (red lines) based on the DFT optimized structure. (D) Comparison between
705 structural refined (red line) and experimental As *K*-edge XANES spectra (black
706 circle-line) of AT-pH 7sample. (E) The FPMS refined cluster of $HAsO_4^{2-}$ doped
707 barite.
708

709 **TABLES**

710 **TABLE 1.** The shell-fit results for the As *K*-edge EXAFS of the reference materials
711 and the As(V)-doped barite. CN refers to the coordination number. R_{path} is the
712 interatomic distance. σ^2 is the Debye-Waller parameter. ΔE is the energy-shift
713 parameter and χ^2_{red} is the reduced chi-square. *R*-factor is the mean-square misfit
714 between the measured and the modeled data. The fitted *k* was set to 3 – 13.5 $Å^{-1}$.
715 Accordingly, the number of independent points (N_{idp}) and variables (N_{var}) were 19.75
716 and 7, respectively. S_0^2 was set 0.95.

Sample	Path	CN	R_{path} (Å)	σ^2 ($Å^2$)	ΔE (eV)	χ^2_{red}	*R*-factor
$BaHAsO_4 \cdot H_2O$	As-O	3	1.68±0.007	0.0016±0.0003	7.5±1.0	93	0.012
	As-OH	1	1.76±0.007	0.0016±0.0003			
	As-Ba1	1	3.65±0.029	0.0113±0.0028			
	As-Ba2	1	3.94±0.029				
	As-Ba3	1	3.98±0.029				
	As-Ba4	1	4.02±0.029				
	As-Ba5	1	4.16±0.029				
$Ba_3(AsO_4)_2$	As-O	4	1.70±0.006	0.0014±0.001	2.7±2.1	141	0.020
	As-Ba1	3	3.58±0.060	0.0067±0.003			
	As-Ba2	3	3.73±0.060				
AT-pH 3	As-O	3	1.67±0.031	0.0017±0.0003	6.7±1.6	9	0.025
	As-OH	1	1.75±0.031	0.0017±0.0003			
	As-Ba1	3	3.53±0.013	0.0128±0.0033			
	As-Ba2	2	3.74±0.013				
	As-Ba3	1	3.84±0.013				
AT-pH 7	As-O	3	1.67±0.003	0.0014±0.0002	7.6±1.1	23	0.018
	As-OH	1	1.75±0.003	0.0014±0.0002			
	As-Ba1	3	3.53±0.035	0.0349±0.0418			
	As-Ba2	2	3.74±0.035				
	As-Ba3	1	3.84±0.035				
AT-pH 10	As-O	3	1.67±0.046	0.0012±0.0002	7.5±1.0	24	0.015
	As-OH	1	1.76±0.046	0.0012±0.0002			
	As-Ba1	3	3.53±0.037	0.0135±0.0028			
	As-Ba2	2	3.74±0.078				
	As-Ba3	1	3.85±0.078				

717

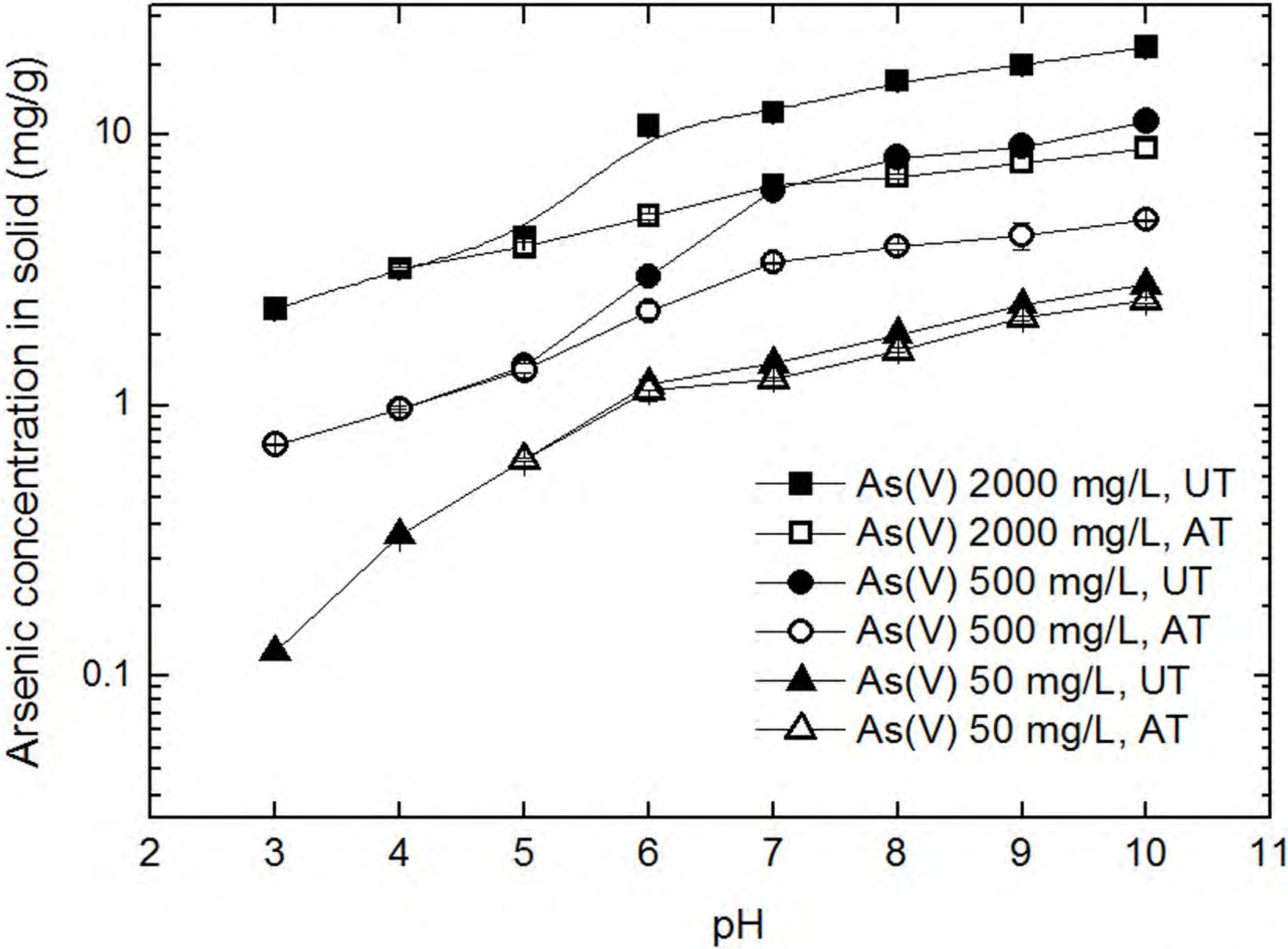
Arsenic concentration in solid (mg/g)
10
1
0.1
2
3
4
5
6
7
8
9
10
11
pH
As(V) 2000 mg/L, UT
As(V) 2000 mg/L, AT
As(V) 500 mg/L, UT
As(V) 500 mg/L, AT
As(V) 50 mg/L, UT
As(V) 50 mg/L, AT

Fig 1

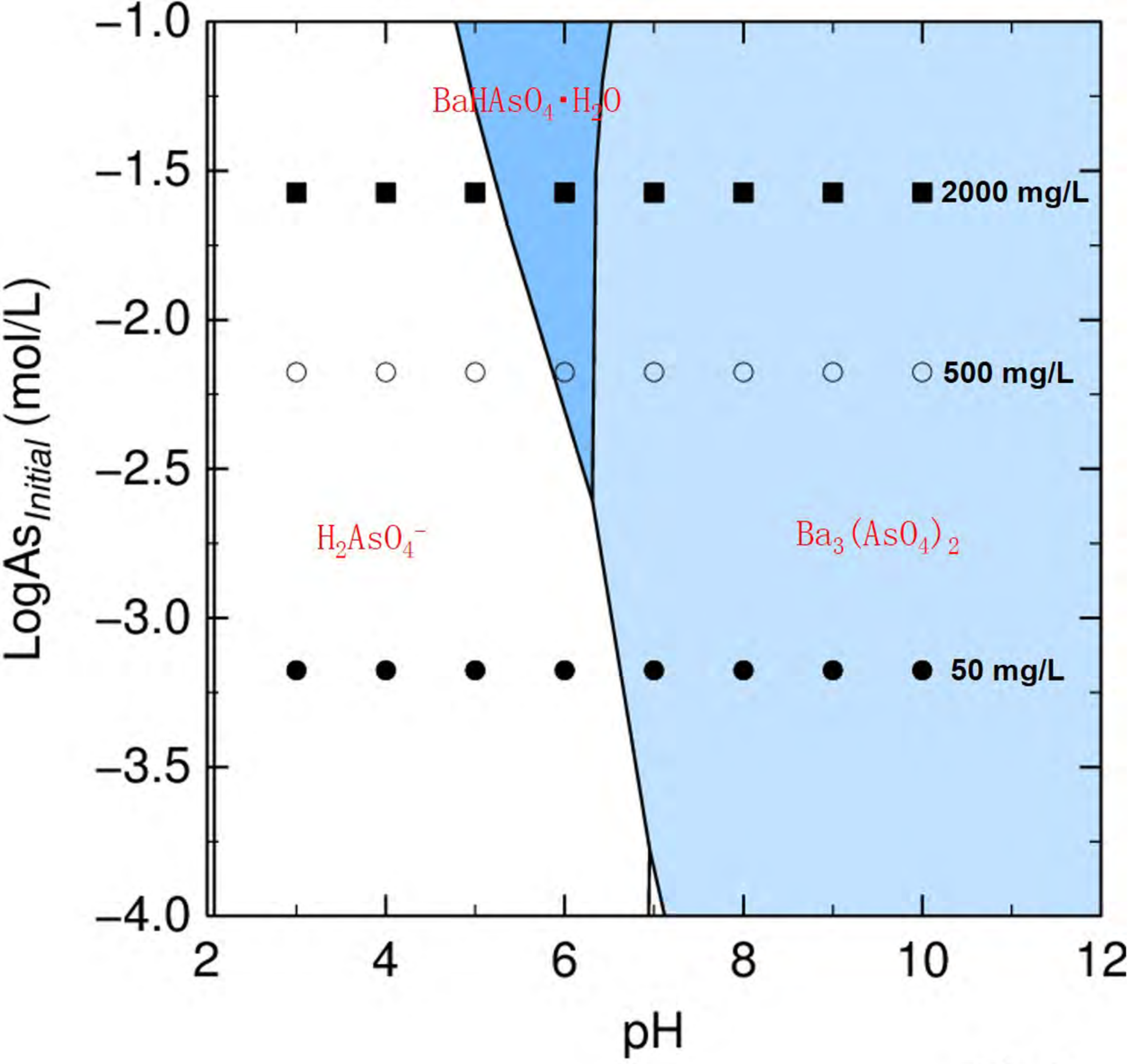
BaHAsO4·H2O
H2AsO4−
Ba3(AsO4)2
2000 mg/L
500 mg/L
50 mg/L
LogAsInitial (mol/L)
pH
−1.0
−1.5
−2.0
−2.5
−3.0
−3.5
−4.0
2
4
6
8
10
12

Fig 2

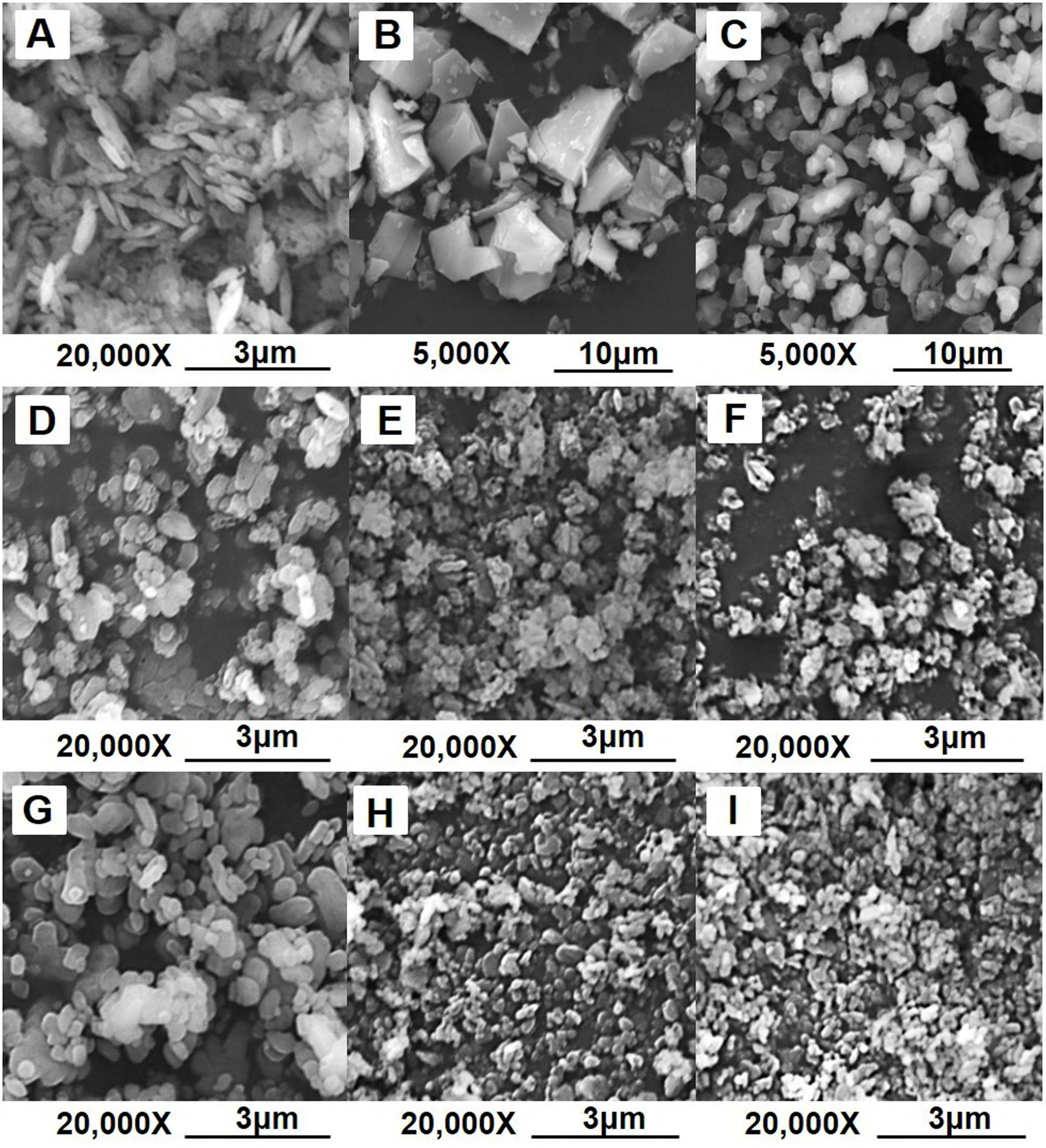
A
B
C
20,000X
3µm
5,000X
10µm
5,000X
10µm
D
E
F
20,000X
3µm
20,000X
3µm
20,000X
3µm
G
H
I
20,000X
3µm
20,000X
3µm
20,000X
3µm

Fig 3

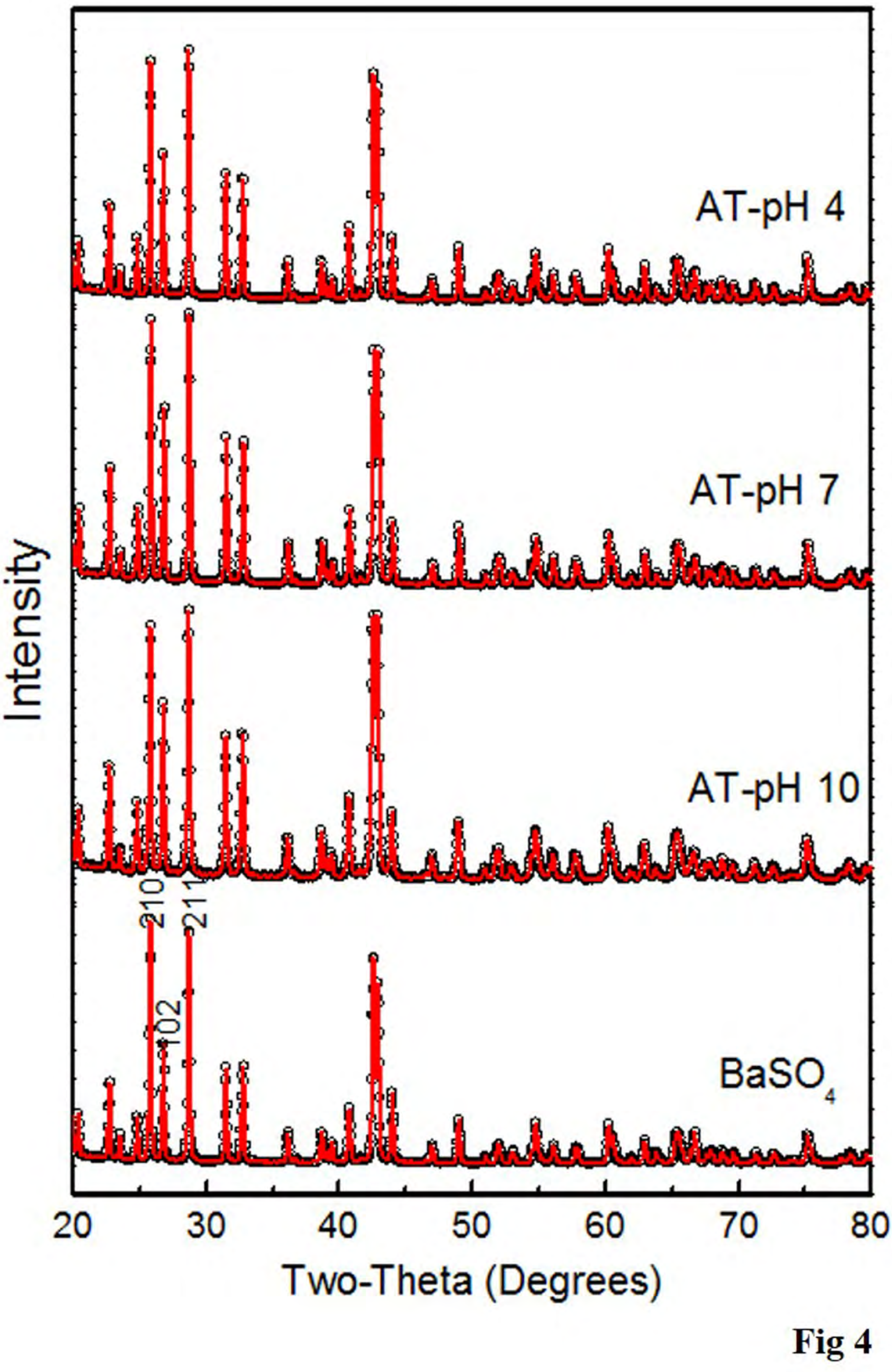
AT-pH 4
AT-pH 7
AT-pH 10
BaSO4
Intensity
210
211
102
20
30
40
50
60
70
80
Two-Theta (Degrees)

Fig 4

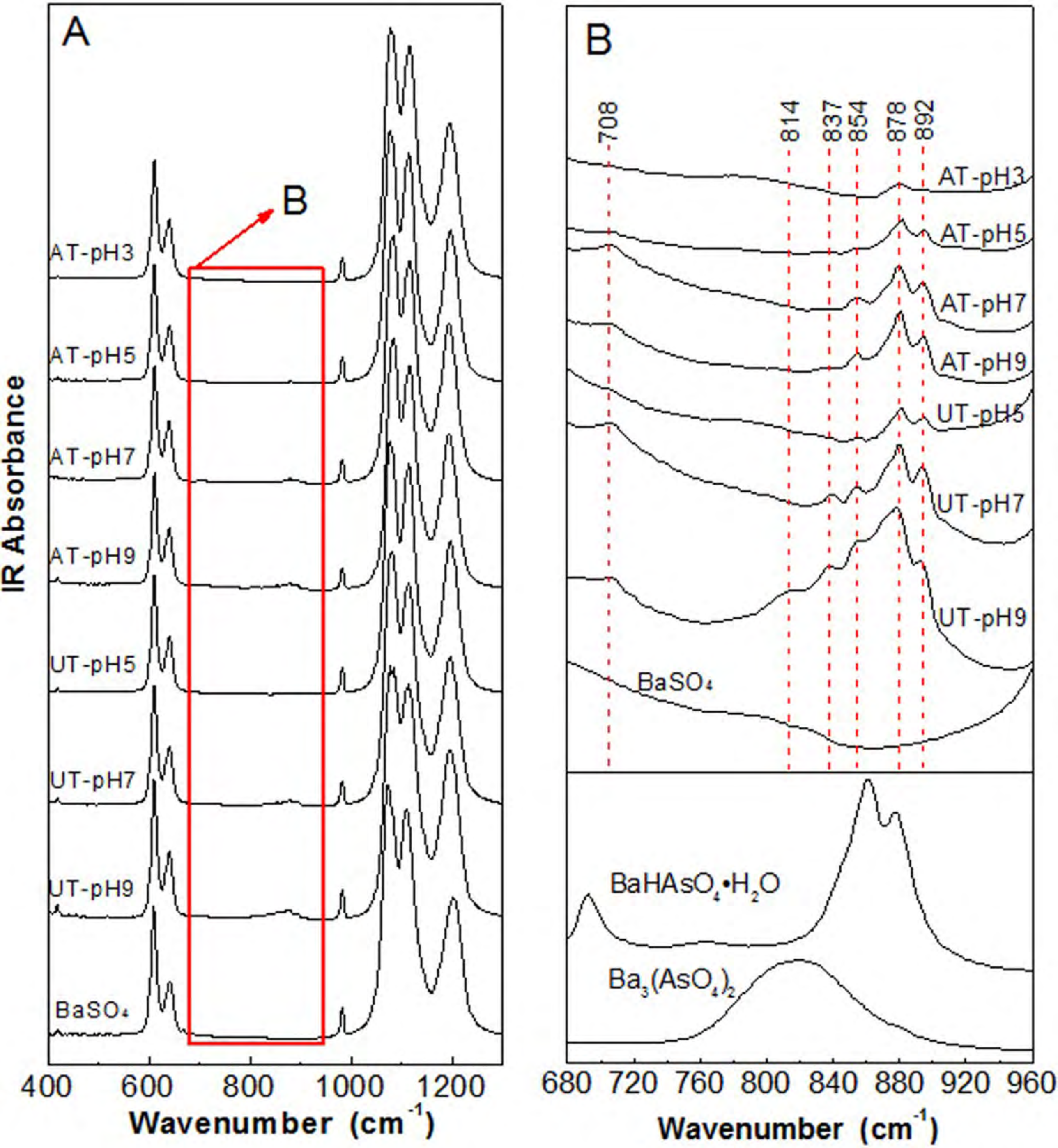
A
B
AT-pH3
AT-pH5
AT-pH7
AT-pH9
UT-pH5
UT-pH7
UT-pH9
BaSO4
IR Absorbance
400
600
800
1000
1200
Wavenumber (cm-1)
B
708
814
837
854
878
892
AT-pH3
AT-pH5
AT-pH7
AT-pH9
UT-pH5
UT-pH7
UT-pH9
BaSO4
BaHAsO4•H2O
Ba3(AsO4)2
680
720
760
800
840
880
920
960
Wavenumber (cm-1)

Fig 5

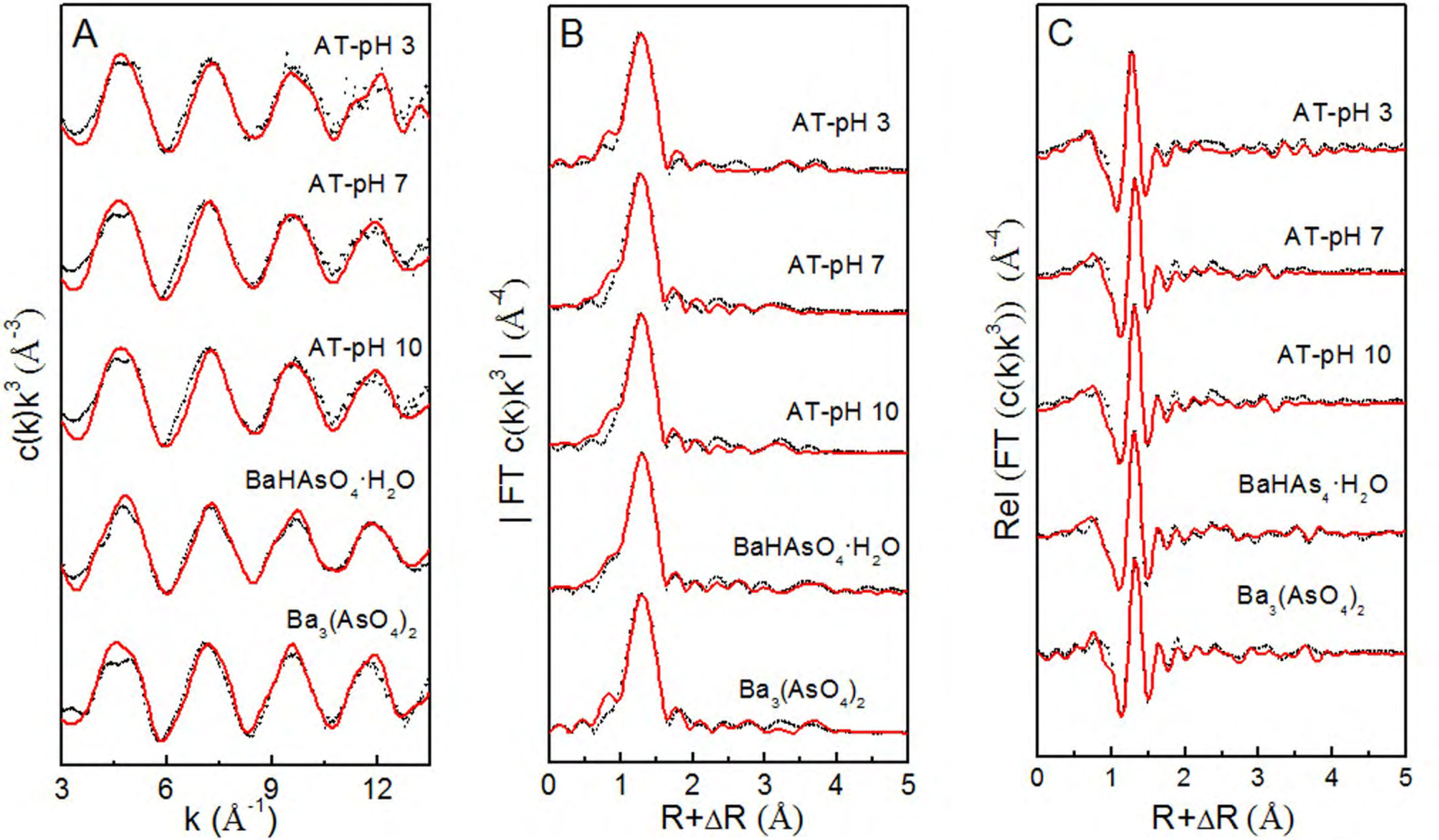
A
AT-pH 3
AT-pH 7
AT-pH 10
BaHAsO4·H2O
Ba3(AsO4)2
c(k)k3 (Å-3)
3
6
9
12
k (Å-1)
B
AT-pH 3
AT-pH 7
AT-pH 10
BaHAsO4·H2O
Ba3(AsO4)2
| FT c(k)k3 | (Å-4)
0
1
2
3
4
5
R+ΔR (Å)
C
AT-pH 3
AT-pH 7
AT-pH 10
BaHAs4·H2O
Ba3(AsO4)2
Rel (FT (c(k)k3)) (Å-4)
0
1
2
3
4
5
R+ΔR (Å)

Fig 6

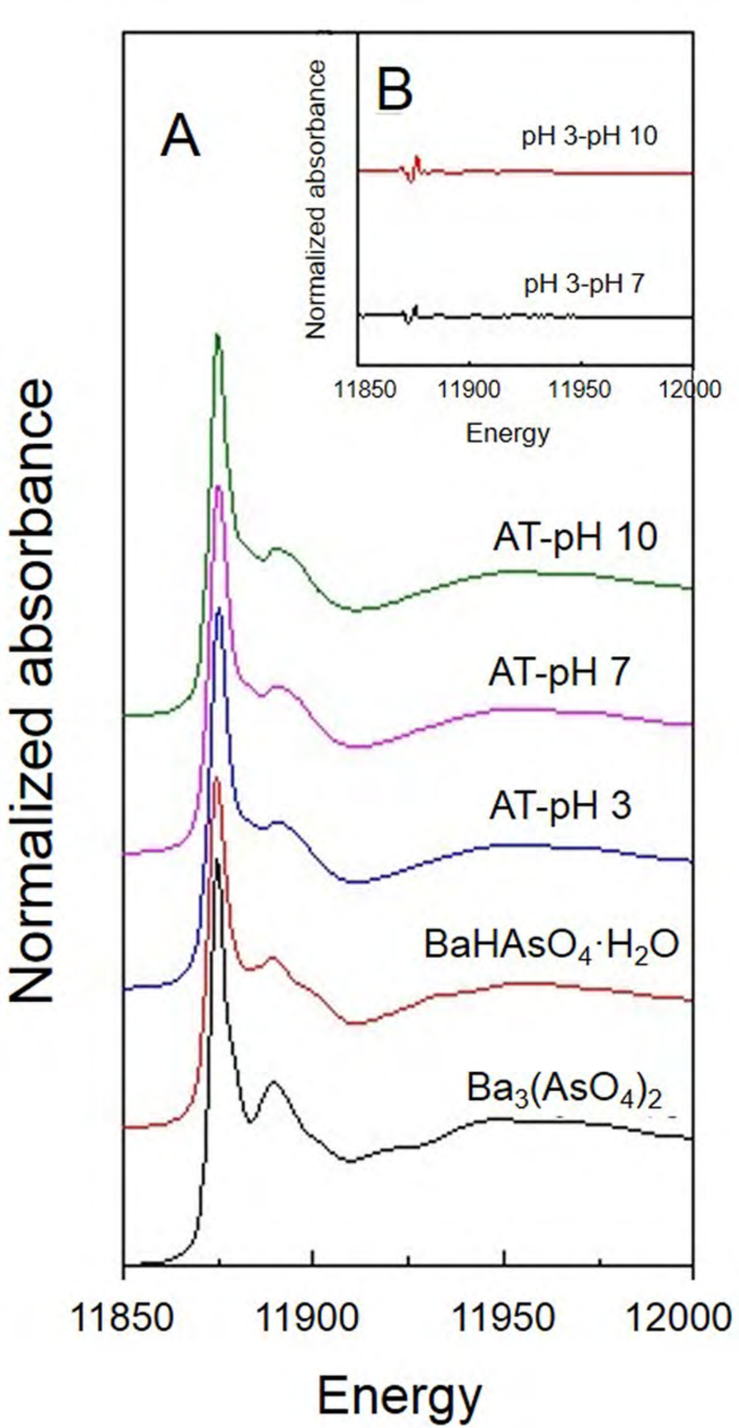
A
B
Normalized absorbance
pH 3-pH 10
pH 3-pH 7
11850
11900
11950
12000
Energy
AT-pH 10
AT-pH 7
AT-pH 3
BaHAsO4·H2O
Ba3(AsO4)2
Normalized absorbance
11850
11900
11950
12000
Energy

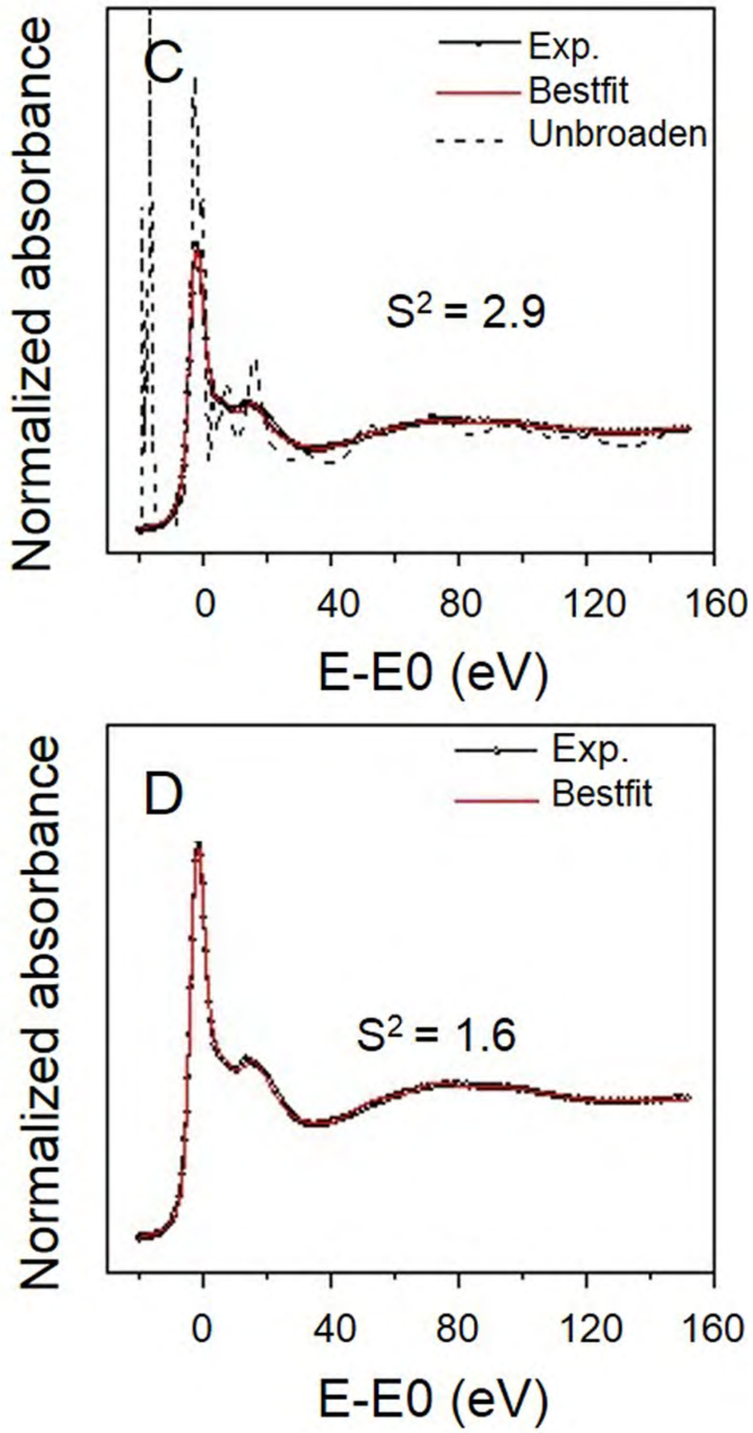
C
Exp.
Bestfit
Unbroaden
S2 = 2.9
Normalized absorbance
0
40
80
120
160
E-E0 (eV)
D
Exp.
Bestfit
S2 = 1.6
Normalized absorbance
0
40
80
120
160
E-E0 (eV)

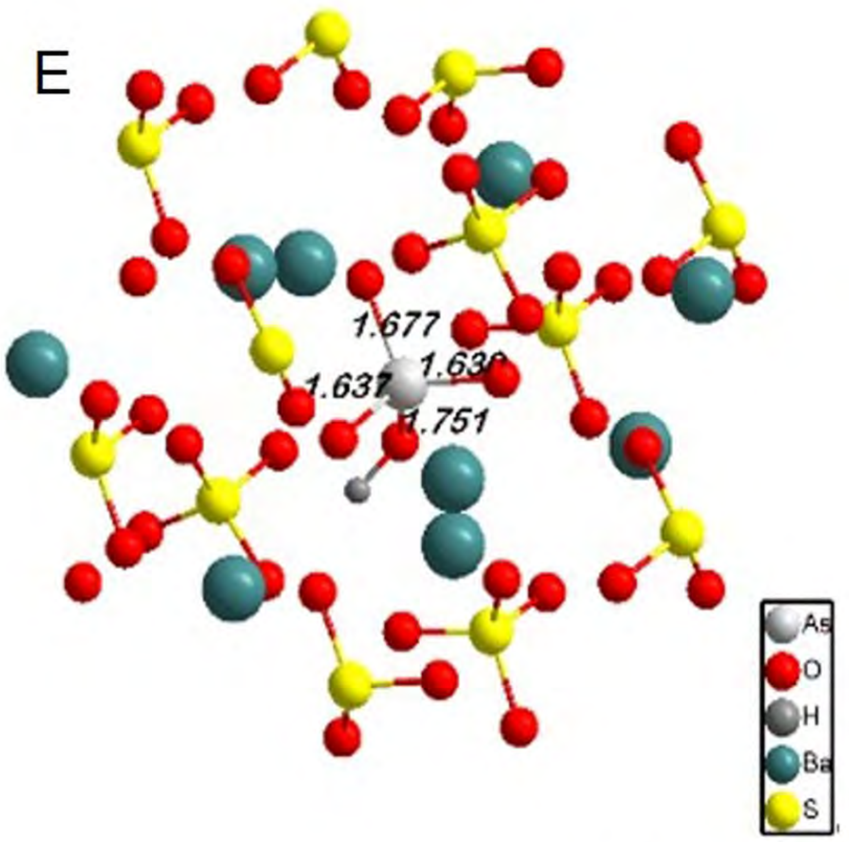
E
1.677
1.631
1.751
As
O
H
Ba
S

Fig 7